Developing a Modular Tool to Simulate Regeneration Power Potential Using Orographic Wind-hovering UAVs

Gossye, M.; Hwang, S.; Remes, B. D.W.

DOI
10.1142/S2301385022410047

Publication date
2022

Document Version
Accepted author manuscript

Published in
Unmanned Systems

Developing a Modular Tool to Simulate Regeneration Power Potential Using Orographic Wind-hovering UAV's

M. Gossye[a,*] S. Hwang[a], and B.D.W. Remes[a]

[a] *MAVLab, Delft University of Technology, Kluyverweg 1, 2629HS Delft, the Netherlands*
E-mail: midasgossye@gmail.com

Applications of Unmanned Aerial Vehicles (UAV's) are often limited by flight endurance. To address the limitation of endurance, we propose a regenerative soaring method in this paper. The atmospheric energy from updrafts generated by obstacles such as hills and ships can be harvested by UAV's using a regenerative electric drivetrain. With fixed-wing aircraft, the vehicle can hover with specific wind conditions, and the battery can be recharged in the air while wind hovering. In order to research the feasibility of this regenerative soaring method, we present a model to estimate hovering locations and the amount of extractable power using the proposed method. The resulting modular regeneration simulation tool can efficiently determine the possible hovering locations and provide an estimate of the power regeneration potential for each hovering location, given the UAV's aerodynamic characteristics and wind-field conditions. Furthermore, a working regenerative drivetrain test setup was constructed and characterised that showcased promising conversion efficiencies and can be incorporated into existing UAV's easily.

Keywords: Wind-hovering; Regenerative soaring; Regenerative drivetrain

1. Introduction

UAV's are performing more and more diverse missions every year, but are often limited by the maximum achievable endurance and/or range. Using the principle of orographic soaring to extend the range and endurance of UAV's has already been extensively researched, often based on techniques used by various bird species that have been observed.[1,2] However, conventional orographic soaring techniques do have some limitations that limit their usability in certain environments and conditions.

With traditional soaring methods, the only energy-storage mediums are the potential energy (altitude) and kinetic energy (airspeed) of the aircraft. The associated aircraft state variables, altitude & airspeed, are often desired to stay constant to be able to take advantage of the favourable conditions to gain energy from the atmosphere.[3] A great example of this is when one is, for instance, soaring upwind along a ridge trying to take advantage of the updrafts it generates. It is possible to store the gained energy in the form of altitude, but the higher the altitude, the weaker the updrafts are from the obstacle. At a certain altitude, the updrafts become so weak that the glider is barely able to maintain altitude without losing airspeed. Once this "ceiling altitude" is reached, it is not possible to store any more energy. It is possible to trade the potential energy for kinetic energy, and dive back down to the original altitude while gaining airspeed. The aircraft is now positioned once again in a region with stronger updrafts. However, due to the increased airspeed, the glider has a higher sink-speed which may render it unable to gain energy from the updrafts anymore.

Regenerative soaring introduces another energy storage medium to store harvested energy from the environment. The regenerative soaring method was first proposed by Paul MacCready already back in 1998 .[4] Instead of having to change the altitude and/or airspeed to be able to store energy, an on-board energy accumulator in the form of a rechargeable battery can harvest the energy through the use of a regenerative drivetrain. This means that the aircraft can stay positioned in the altitude region where the most favourable updrafts are present, and keep its optimum airspeed.

One problem with the suggested regenerative orographic soaring methods is that a long ridge or hill range is required to take advantage of this, such that the aircraft can fly straight along the ridge in the most favourable updraft regions for an extended period of time. It would be beneficial if small UAV's could also use the updrafts present around smaller, single objects such as a small hill, a building or a ship on the open sea. This could be achieved by altering the orographic regenerative soaring methods by applying a technique called wind hovering or static hovering.

Achieving static hovering while using the orographic soaring method (called wind hovering) is a topic found in

*Delft, the Netherlands

a minimal amount of research.

Fisher [5] introduced the concept of a "feasible soaring region", a spatial region inside a wind-field where wind hovering is possible for a given wind-speed. A point in the wind-field is deemed feasible for wind hovering if the local vertical wind component/updraft velocity is larger or equal than the minimum sink speed of the aircraft when flying at zero ground speed in the wind field. In their paper, the feasibility of having a fixed-wing UAV autonomously hover in the updraft region of a hill and a building was investigated. The paper concluded with the experimental results proving that a small UAV can indeed apply wind-hovering techniques to statically hover in the favourable updraft region. Our research tries to determine if this wind hovering UAV concept can be extended by adding a regenerative drivetrain, which would in theory combine both the advantages of wind hovering and regenerative soaring techniques. In order to research the feasibility and achievable power levels of this concept, a simplified model was created that can estimate the best case available regen power while hovering, given the aerodynamic parameters of the UAV and the flow conditions of the wind-field. Furthermore, a test-setup was devised to measure the real-life efficiency of a regenerative drivetrain with standard components such as a Brushless DC electric (BLDC) motor and Lithium Polymer (LiPo) battery typically found on small electric UAV's.

The remainder of this paper is structured as follows: Section 2 introduces the wind field estimation method, Section 3 describes how to calculate extractable power generated by the wind field, Section 4 presents how the feasible soaring locations and generated power at each location are determined. Section 5 presents some details on the regenerative drivetrain test setup and results. Finally, Section 6 gives a summary of the presented work and discusses future work that can expand this concept.

2. Wind-field estimation

To be able to determine the power available in the wind-field, it is first vital to have a good understanding of the wind-field. To achieve this, a wind-field estimation tool is required that can simulate the flow around various simple obstacles. The following subsections will describe what methods are available to achieve this and how the wind-field estimation program was implemented.

2.1. *Methods*

There exist numerous methods to estimate the behaviour of air around obstacles, greatly varying in complexity and required computational power. The most common choice lately has been to use a complex Computational Fluid Dynamics (CFD) simulation package like ANSYS fluent, openFOAM, etc. The CFD simulations performed with these packages require a large amount of computational power and are very complex to set-up. It was opted to first search for another method as a basis of the wind-field estimator. Langelaan used a simplified potential flow method to find the wind field upwind of an idealised circular shaped hill, as was presented in [6], to gain a better understanding of the general behaviour of the wind-field and to estimate the ideal location relative to the circular hill for ridge soaring. This methodology sparked the idea to use potential flow theory to estimate the flow field present upwind of the hill.

2.2. *Potential flow estimator*

The standard potential flow equations describing the idealised flow around circular and oval shaped obstructions were used as a basis.

The equations used to determine the flow-field are listed below, with U_∞ being the free-stream velocity, R the radius of the circular hill and r the distance between the aircraft and the centre of the hill. θ represents the angle between the horizontal axes and the radial of the aircraft (see Figure 1):

$$u_r = \left[1 - \frac{R^2}{r^2}\right] U_\infty \cos\theta \tag{1}$$

$$u_\theta = -\left[1 + \frac{R^2}{r^2}\right] U_\infty \sin\theta \tag{2}$$

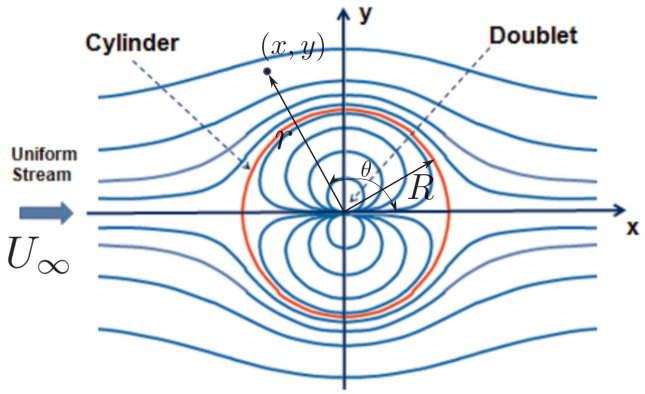

Fig. 1: Potential flow field around cylinder

Transforming the polar velocity components into cartesian velocity components results in the following velocity functions for the x and y components:

$$u_x = \cos\theta \cdot u_r - \sin\theta \cdot u_\theta \tag{3}$$

$$u_y = \sin\theta \cdot u_r + \cos\theta \cdot u_\theta \tag{4}$$

$$with \quad \theta = \arctan\frac{y}{x} \tag{5}$$

Another set of equations for oval shaped hills can also be selected, which correspond to the equations representing the flow-field over a rankine oval, as described in [7]:

$$x_{stag}^2 - a^2 - \frac{ma}{\pi U_\infty} = 0 \tag{6}$$

$$\Leftrightarrow m = \frac{\pi U_\infty}{a}(x_{stag}^2 - a^2) \tag{7}$$

$$u_x(x,y) = U_\infty + \frac{m}{2\pi}\left[\frac{x+a}{(x+a)^2+y^2} - \frac{x-a}{(x-a)^2+y^2}\right] \tag{8}$$

$$u_y(x,y) = \frac{my}{2\pi}\left[\frac{1}{(x+a)^2+y^2} - \frac{1}{(x-a)^2+y^2}\right] \tag{9}$$

Where the x-coordinate of the stagnation point x_{stag} and the x-coordinate of the focal point a determine the geometry of the oval shaped hill.

These equations were then altered with a simplified boundary/shear layer model equation to include an estimate of the Atmospheric Boundary Layer.

Equation 10 shows the used model that alters the vertical wind-speed distribution with a logarithmic function to try to estimate the Atmospheric Boundary Layer.

One problem arises by using this simple model to estimate the varying wind speeds in the boundary layer, the function is only able to estimate the boundary layer effects to the horizontal wind-speed over flat terrain. It has been proven though that the log wind-profile can produce accurate results even above non-flat terrain in certain circumstances at higher altitudes above the obstacle.[8] The log wall function can certainly be applied to the regions of the flow that are not greatly affected by the presence of the hill (mainly upwind of the hill-side). The proposed boundary layer model will however most likely not predict the boundary layer effects close to the hill surface. It was still opted to use this model for the entire hill region since the resulting flow patterns are more closely resembling real-life wind conditions where the flow velocity decreases close to the surface due to friction. If more accurate flow behaviour needs to be predicted close to the surface of the hill, a CFD simulation including models for laminar and turbulent boundary layer behaviour would be more applicable.

$$u(z_2) = u(z_1)\frac{\ln\left((z_2-d)/z_0\right)}{\ln\left((z_1-d)/z_0\right)} \tag{10}$$

3. Power contours

Now that a wind field estimate is available around differently sized obstacles, it is time to determine the feasible power that can be extracted at each point.

Before going into the details of the ability of the UAV to perform wind hovering at each location, it is helpful to first estimate the theoretical maximum power that can be extracted at each location assuming the UAV can maintain to hover at that location indefinitely. In this case, the energy harvesting UAV can essentially be modelled as a Horizontal Axis Wind Turbine (HAWT) where the upstream wind velocity is equal to the total wind velocity at the location of the UAV in the wind field. This is not totally accurate, since this assumes that the upstream wind velocity is constant along the axis of the propeller, but since the propeller dimensions of small UAV are at least an order of magnitude smaller than the obstacle dimensions it can be assumed that this will only have a very minor effect.

To be able to determine the theoretical maximum power that a HAWT can extract from the wind stream, it is evident to first have a closer look into the so called Betz law:

3.1. *Betz law*

One of the most famous theories concerning wind turbine theory is the Betz law (also called Betz condition or limit).

Simply put, it states that even an ideal wind turbine that contains no centre hub and has an infinite number of blades that cause no additional drag (e.g. skin friction drag) can only extract roughly 59 % of the power available in the wind stream.[9] To be able to achieve a continuous power extraction flow, it is evident that a continuous mass flow of air must pass through the propeller/turbine disc. For this to occur, both the incoming and outgoing flow must have a positive flow velocity. If, hypothetically, the turbine was able to extract all of the available energy from the incoming flow, the flow past the disc area should have a velocity of zero (otherwise there would still be unextracted energy present). Having a zero fluid flow velocity at the exit of the turbine, directly means that no mass flow can be present, so no power can be extracted at these conditions.

Using the continuity equation, Euler's theorem and kinetic energy equations the following ideal power limit following the Betz law can be derived [9]:

$$P_{ideal} = \frac{16}{27}\frac{1}{2}\rho S_{turb} V_{air}^3 \tag{11}$$

This first estimate for the maximum theoretical power can be used as a basis to generate the power contours for the wind field. The following assumptions have to be kept in mind though:

- The wind turbine is assumed to not have a hub, the entire disc area region only contains blades
- It has an infinite number of blades that cause no additional drag (e.g. skin friction drag, induced drag due to tip vortices)
- The incoming flow is assumed to be constant, laminar and axial to the wind turbine axis
- No swirl is generated, the outgoing flow is also flowing axial to the wind turbine axis
- The air is considered to be an incompressible fluid

3.2. *Using Betz law to generate potential power contours*

Figure 2 shows the ideal maximum power at every location in the wind field that could be extracted from a $15\,\mathrm{m\,s^{-1}}$ free-stream velocity over a circular hill section with a radius of 50 m for a wind-turbine with a rotor disc area of $0.1\,\mathrm{m^2}$. It basically represents the absolute ideal maximum power that a regenerating UAV could achieve at every point in the wind field if static hovering can be achieved at that point and if the turbine can operate at its maximum power operating point, which will obviously not be the case for the majority of the wind field.

It is logical that the highest ideal power estimates are located directly above the hill since this is where the wind speeds are the highest (for the idealised potential flow case). It can be seen however that close to the surface of the hill the power figure is lower since this region has a lower velocity due to the added boundary layer wall function.

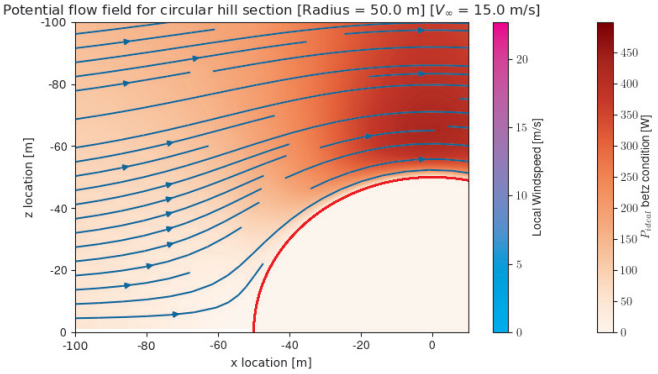

Fig. 2: Ideal power contour plot for a $15\,\mathrm{m\,s^{-1}}$ free-stream velocity over a circular hill section with a radius of 50 m for a rotor disc area of $0.1\,\mathrm{m^2}$

4. Determining hovering locations & power generation potential

Now that the absolute maximum theoretical power that can be extracted at each point in the wind field is known, the next step is to determine if the UAV can actually hover at that location, and if so, what power fraction should be extracted from the turbine to generate the required drag equalising the "thrust" generated by gravity, to enable the hovering to be stable?

To be able to answer this question, the equations governing the longitudinal flight dynamics of a hovering UAV needs to be studied.

4.1. *Longitudinal hovering flight dynamics*

The following equations (Equations 12, 13 and 14) express the system of differential equations for longitudinal flight dynamics (following from the Free-Body Diagram (FBD) given in Figure 3), including a non-zero wind, in the air-path reference system, as stated in the avian inspired energy harvesting paper [10]:

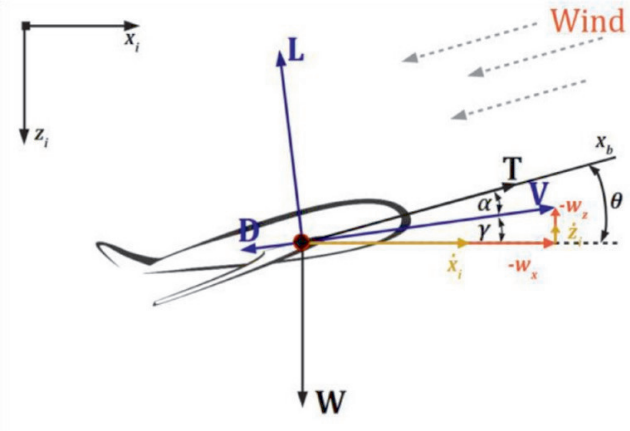

Fig. 3: FBD Air path reference system longitudinal flight dynamics (courtesy of [10])

$$T - D - W\sin\gamma = \frac{W}{g}\left(\dot{V}_{air} + \dot{u}_x\cos\gamma - \dot{u}_z\sin\gamma\right) \tag{12}$$

$$-L + W\cos\gamma = \frac{W}{g}\left(-\dot{V}_{air}\dot{\gamma} + \dot{u}_x\sin\gamma + \dot{u}_z\cos\gamma\right) \tag{13}$$

$$M = \ddot{\theta} I_{yy} \tag{14}$$

The equilibrium equations governing the balance of forces required for a UAV to hover in a steady state can be easily derived by setting the time derivative of the airspeed and both wind speed components (horizontal and vertical) to zero. The thrust force is also replaced with a (negative) turbine drag force which will represent the additional variable drag generated by propeller/motor drivetrain that can act as a turbine. To avoid possible confusions between the total drag force (encompassing both the aircraft and turbine drag forces) and the drag force purely generated due to the aerodynamic properties of the aircraft, the symbol D which represented the latter was replaced by D_{AC}. Lastly, it is assumed that all of the forces acting on the aircraft are acting at the CG, meaning no moments are generated. This results in the following system of equations:

$$\begin{cases} -D_{turb} - D_{AC} - W\sin\gamma &= 0 \\ -L + W\cos\gamma &= 0 \end{cases} \tag{15}$$

An altered FBD which reflects the changes and simplifications made is shown in Figure 4.

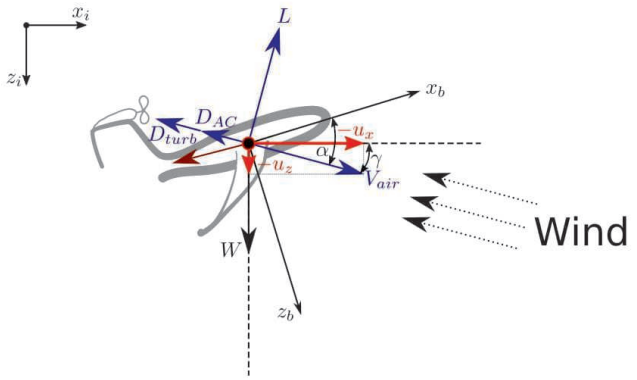

Fig. 4: FBD Air path reference system longitudinal hovering flight dynamics

4.2. *Estimating turbine drag*

Assuming that the turbine behaves as an ideal wind turbine as discussed in Subsection 3.1, it can be assumed that the wind only exerts a net axial force on the rotor. This means the useful power that the wind turbine extracts can be written as the product of this axial force (D_{turb}) and the air velocity at the rotor disc/turbine (V_{turb}): $P_{turb} = D_{turb} \cdot V_{turb}$. Furthermore, when the rotor is operating at the theoretical maximum efficiency conditions Betz proved that the air velocity at the rotor disc/turbine must be equal to two thirds of the incoming air velocity.[9] Using these equations and observations, it is possible to derive a simple expression for the estimated drag produced by an ideal turbine which is shown below (see Figure 5 for diagram with variables):

$$P_{ideal} = \frac{16}{27}\frac{1}{2}\rho S_{turb} V_{air}^3 \tag{16}$$

$$D_{turb} = \frac{P_{ideal}}{V_{turb}} \tag{17}$$

$$V_{turb} = \frac{2}{3} V_{air} \tag{18}$$

Substituting Equation 18 in Equation 17:

$$D_{turb} = \frac{P_{ideal}}{\frac{2}{3} V_{air}} \tag{19}$$

Finally. substituting Equation 19 in Equation 16 results in an equation expressing the estimated turbine drag (D_{turb}) in terms of incoming airspeed (V_{air}) and rotor disc area (S_{turb}):

$$\boxed{D_{turb} = \frac{1}{2}\frac{2}{9}\rho S_{turb} V_{air}^2} \tag{20}$$

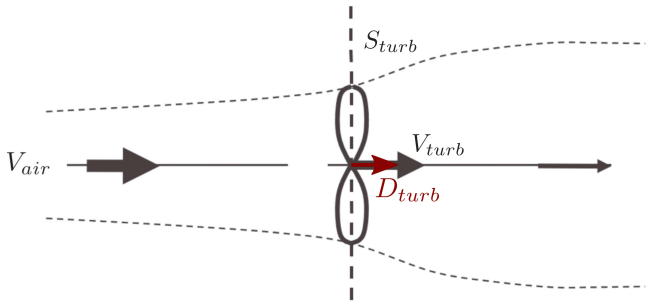

Fig. 5: Ideal wind turbine diagram

4.3. *Finding the required lift and drag coefficients for hovering*

Now that both the systems of equations describing the force equilibrium during hovering flight and an estimate for the turbine drag are found, it is possible to derive a set of equations that determine the required lift and drag coefficients to enable static hovering.

Following from the system of equations that describes the force equilibrium during hovering flight derived in Subsection 4.1 (Equation 15), the required lift and drag terms can be expressed as follows:

$$\begin{cases} L & = W\cos\gamma \\ D_{turb} + D_{AC} & = -W\sin\gamma \end{cases} \tag{21}$$

Rewriting this system of equations in terms of the lift and drag coefficients, substituting D_{turb} with Equation 20 and dividing both sides by $\frac{1}{2}\rho V_{air}^2 S$ results in the following system of equations:

$$\begin{cases} C_{L_{hover}} & = \frac{W}{\frac{1}{2}\rho V_{air}^2 S}\cos\gamma \\ \frac{2}{9}\frac{S_{turb}}{S} + C_{D,AC_{hover}} & = -\frac{W}{\frac{1}{2}\rho V_{air}^2 S}\sin\gamma \end{cases} \tag{22}$$

The resulting non-dimensionalised contribution of the turbine to balance the horizontal force equilibrium (the bottom row of Equation 22), $\frac{2}{9}\frac{S_{turb}}{S}$, can be thought of being the maximum achievable drag coefficient of the turbine, since multiplying this figure by $\frac{1}{2}\rho V_{air}^2 S$ results in the ideal maximum drag caused by the turbine. Setting $C_{D_{turb}} = \frac{2}{9}\frac{S_{turb}}{S}$ results in the following system of equations:

$$\begin{cases} C_{L_{hover}} & = \frac{W}{\frac{1}{2}\rho V_{air}^2 S}\cos\gamma \\ C_{D_{turb}} + C_{D,AC_{hover}} & = -\frac{W}{\frac{1}{2}\rho V_{air}^2 S}\sin\gamma \end{cases} \tag{23}$$

Next, the sine and cosine of the flight path angle (γ) can be substituted with the fractions $\frac{u_z}{V_{air}}$ and $\frac{u_x}{V_{air}}$ respectively. This can be done because the velocity of the UAV with respect to the inertial reference frame is assumed to be zero during stable hovering. This means that the airspeed vectors magnitude and direction is purely determined by the local wind speed vectors (see Figure 4).

$$\begin{cases} C_{L_{hover}} & = \frac{W}{\frac{1}{2}\rho V_{air}^2 S}\frac{u_x}{V_{air}} \\ C_{D_{turb}} + C_{D,AC_{hover}} & = -\frac{W}{\frac{1}{2}\rho V_{air}^2 S}\frac{u_z}{V_{air}} \end{cases} \tag{24}$$

Finally, if the lift-drag polar can be estimated using the following standard equation relating the drag and lift coefficient to each other:

$$C_{D,AC} = C_{D_0} + \frac{C_L^2}{\pi A e} \tag{25}$$

And substituting this equation in Equation 24:

$$\begin{cases} C_{L_{hover}} & = \frac{W}{\frac{1}{2}\rho V_{air}^2 S}\frac{u_x}{V_{air}} \\ C_{D_{turb}} + C_{D_0} + \frac{C_{L_{hover}}^2}{\pi A e} & = -\frac{W}{\frac{1}{2}\rho V_{air}^2 S}\frac{u_z}{V_{air}} \end{cases} \tag{26}$$

This leaves a system of equations that can easily be solved for both the required lift coefficient ($C_{L_{hover}}$), and turbine drag coefficient $C_{D_{turb}}$ if the local air speed (which is equal to the wind speed magnitude during hovering), horizontal and vertical wind speed components are known.

Some important observations can be made from the final equations:

- The required lift coefficient, determined by the first part of Equation 26, should be less than the maximum lift coefficient of the aircraft. If this would not be the case, the aircraft would effectively stall when trying to achieve these conditions.
- The drag that the clean aircraft itself can provide is fixed by the required operating point on the lift-drag polar. If the required drag coefficient is lower than this value, the aircraft will not be able to achieve hovering equilibrium, even if the turbine is fully switched off or assumed to not be present;
- At specific wind speed and direction conditions, the clean aircraft will be able to provide just the right amount of drag at a certain required lift coefficient to satisfy both equilibrium equations, the turbine doesn't need to be switched on, and no power can be regenerated, since $C_{D_{turb}}$ will have to be equal to 0.
- At wind conditions where more drag is required than the clean aircraft itself can provide, the turbine needs to be switched on to close the "drag deficit" and equalise both terms of the second part of Equation 26. If the required extra drag from the turbine is less than its ideal maximum, the regen drivetrain should regulate the drawn power from the turbine in such a way that the drag provided by the turbine satisfies the equations.
- There exist another specific set of wind conditions where the required drag from the turbine to achieve hovering equilibrium will be equal to the maximum drag that the turbine ideally can provide. Note that although the maximum amount of power (imposed by the Betz limit) that can be drawn from the turbine in this scenario at the specific conditions, it is not necessarily the optimum resulting in the maximum amount of regeneration power, since the regeneration power also depends on the wind speed and other locations in the wind-field might exist where not all ideally available power can be extracted, but due to a higher wind speed the total regenerated power potential is still higher.

With the finalised equations for the turbine drag coefficient and above observations in mind, the calculation of the regen power contours can now be performed.

4.4. *Regen power contour calculation*

The finalised equations presented in the previous subsection enable one to determine if static hovering is achievable (given the local wind conditions at a certain point in the wind-field and aircraft parameters). If this is the case, the corresponding static hovering power regeneration potential can be calculated for that point.

The resulting equations can be used to determine both the required lift coefficient ($C_{L_{hover}}$), and combined drag coefficients (one being the turbine drag coefficient $C_{D_{turb}}$, the other being the drag coefficient of the aircraft $C_{D,AC_{hover}}$) to enable stable static hovering.

This function determines if the UAV is theoretically able to statically hover with zero ground speed at each point of the calculated wind field. At each potential hover location, the required additional drag and power needed from the turbine is calculated as well as the angle of attack.

First, the required lift coefficient to satisfy the hovering equilibrium equations is calculated:

$$C_{L_{hover}} = \frac{W}{0.5 \cdot \rho \cdot V_{air}^2 \cdot S} \cdot \frac{u_x}{V_{air}} \tag{27}$$

If the resulting lift coefficient is larger than the maximum achievable lift coefficient ($C_{L_{max}}$), the aircraft would stall if it tried to approach the conditions required for hovering and the corresponding point in the wind field will have a zero power regeneration potential using static hovering since hovering cannot be achieved.

Next, the total required drag coefficient to enable hovering ($C_{D_{turb}} + C_{D,AC_{hover}}$) is calculated:

$$C_{D_{turb}} + C_{D,AC_{hover}} = \frac{W}{0.5 \cdot \rho \cdot V_{air}^2 \cdot S} \cdot \frac{u_z}{V_{air}} \tag{28}$$

For the aircraft to be able to achieve static hovering, the combined required drag coefficient can not be smaller than the minimum achievable total drag coefficient. This minimum achievable total drag coefficient is equal to the clean aircraft's drag coefficient, since the least amount of drag will be generated when no additional turbine drag is generated (hence $C_{D_{min}} = C_{D,AC_{hover}} = C_{D_0} + \frac{C_{L_{hover}}^2}{\pi A e}$).

The combined required drag coefficient can also not be larger than the maximum achievable drag coefficient, which is equal to the clean aircraft's drag coefficient plus the maximum achievable turbine drag coefficient. As stated in the previous subsection, the maximum achievable turbine drag coefficient can be estimated using the Betz limit and is equal to $C_{D_{turb,max}} = \frac{2}{9}\frac{S_{turb}}{S}$. Summarising, the acceptable combined required drag coefficient bounds to achieve static hovering leads to the following expression:

$$C_{D_0} + \frac{C_{L_{hover}}^2}{\pi A e} \leq C_{D_{turb}} + C_{D,AC_{hover}} \leq C_{D_0} + \frac{C_{L_{hover}}^2}{\pi A e} + \frac{2}{9}\frac{S_{turb}}{S} \quad (29)$$

If the total required drag coefficient falls within these bounds and the required lift coefficient is not larger than the maximum lift coefficient (as stated earlier), it can be assumed that the aircraft can achieve static hovering, and a valid power regeneration potential can be calculated.

The resulting required turbine drag coefficient to achieve stable static hovering can be calculated as follows:

$$C_{D_{turb,hov}} = C_{D_{turb}} + C_{D,AC_{hover}} - \left(C_{D_0} + \frac{C_{L_{hover}}^2}{\pi A e}\right) \quad (30)$$

The corresponding turbine drag generated during hovering can easily be found by multiplying the turbine drag coefficient with $0.5 \cdot \rho \cdot V_{air}^2 \cdot S$:

$$D_{turb,hov} = 0.5 \cdot \rho \cdot V_{air}^2 \cdot S \cdot C_{D_{turb,hov}} \quad (31)$$

Finally, by rearranging Equation 19 the estimated turbine power can be found:

$$P_{turb.hov} = \frac{2}{3} \cdot V_{air} \cdot D_{turb,hov} \quad (32)$$

4.5. *Results*

By incorporating the finalised turbine drag and power equations and only populating the values for locations where hovering is deemed feasible by satisfying the maximum lift coefficient constraint and conditions set in Equation 29, power contour plots can be generated for any given wind-field. This results in figures like the one shown below (Figure 6):

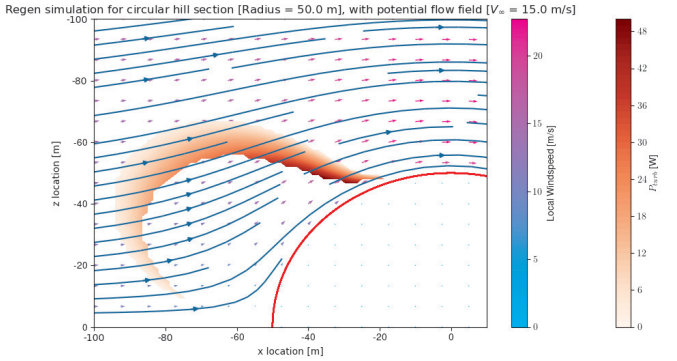

Fig. 6: Regen power contour plot for a $15\,\mathrm{m\,s^{-1}}$ free-stream velocity over a circular hill section with a radius of 50 m for a rotor disc area of $0.1\,\mathrm{m^2}$ using aerodynamic parameters in Appendix A

It can immediately be seen that the estimated maximum amount of power that can be regenerated using the turbine while hovering is roughly 1 order of magnitude lower than the ideal Betz limit power contour graph of the entire wind-field (see Figure 2). The primary reason for this is that the UAV is unable to statically hover with these conditions at the point in the wind-field that has the maximum potential power, which is the point with the highest wind velocity.

Power contour plots were calculated for a range of conditions, such as different wind-speeds, hill-sizes, rotor disc areas, UAV masses, etc. The resulting plots showed the expected behaviour for the change in conditions.

5. Regenerative drivetrain

As was briefly touched upon in the previous section, a special kind of electric drivetrain is required which enables the power flow to be reversed in certain conditions. In normal conditions the battery provides the power to the motor to propel the vehicle, but in the regen mode this power flow is reversed and the motor now acting as a generator can be used as a wind-turbine to supply power back to the battery.

5.1. *Shortcomings of existing setups from prior research*

Most of the previous research into this area focused on determining if this method was suitable to use in light electric road vehicles (e.g. e-scooters) to increase the total driving range of a typical ride that includes sporadic braking. Apart from relative increases in driving ranges, no actual performance data on this setup could be found. It was also identified that in most experiments lead-acid batteries were used which are unsuitable for UAV due to their low energy mass density of around 35-40 Wh/kg (compared to 150-180 Wh/kg for LiPo batteries as described in [11]).

In order to be able to evaluate the performance of using this kind of combined regen controller for the proposed use case in a UAV with LiPo batteries, additional research and tests will be required. Instead of trying to model and develop a prototype regen controller with the required functionality from scratch however, it was decided to first perform a comprehensive search if a possible suitable existing Electronic Speed Controller (ESC) could be found that can be easily reprogrammed and altered to achieve the desired functionality. Once a suitable candidate is found, it can be used to perform tests to try to estimate the efficiency of the regen drivetrain.

5.2. *VESC ESC as combined ESC/regen controller*

After a comprehensive search a possible suitable existing ESC controller was found that even has built-in functionality to be used as a regen controller: the VESC.

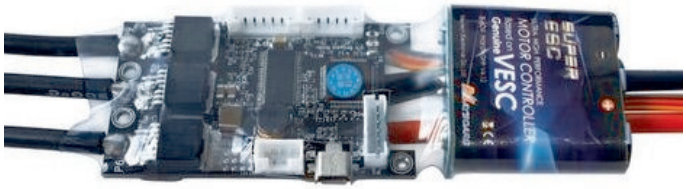

Fig. 7: VESC ESC (courtesy of *electricboardsolutions.com*)

The VESC (depicted in Figure 7) is a fully open-source ESC originally designed to be used in electric skateboards. Over time, it has been further developed to be used in a variety of applications and includes additional features such as datalogging, added control interfaces (such as CAN bus & UART), and (most importantly) regen capability.

The VESC was found to be ideally suited as an all-in-one combined regen controller and ESC for UAV's, due to it's compatibility with recharging LiPo batteries in the regen mode. Because of the open-source nature of the design it is possible to easily alter the firmware and do hardware modifications.

In order to test the performance and power efficiency of the regenerative drivetrain, a test-setup with the VESC will be used that enables the input and output power to be measured while performing the regen function.

5.3. *Test setup description*

The general test-setup diagram is shown in Figure 8. On the left side, a brushless motor is connected to an ESC that drives this motor. The power input of the ESC is connected to a lab bench power supply such that the input voltage can be varied and the output current monitored. The throttle/power setting of the ESC can be adjusted by moving the sticks on a transmitter connected to the receiver (RX) that sends the ESC the required motor throttle signal. This setup basically emulates a propeller providing mechanical power to the shaft of the mechanically coupled brushless motor on the right.

The two brushless motors are connected together with a mechanical shaft coupler. The second brushless motor that is being driven by the first one is connected to the VESC that can be reprogrammed with a custom firmware that employs the regenerative control strategy. This second motor is mounted on a motor benchmarking device called RC benchmark that measures the torque on the motor shaft. The VESC's output is connected to a rechargeable LiPo battery through an ammeter such that the recharging current can be monitored. The VESC has built-in current, voltage and RPM sensors to monitor the brushless motor RPM and braking current, and battery voltage. All of these parameters are logged on a pc by using an interfacing adapter based on an STM32 microcontroller. The desired braking current can be adjusted using a rotary potentiometer on the transmitter that is mapped to a channel and also sent to the RX. The STM32 does the necessary conversion of the PPM signal to the serial commands required by the VESC to set a custom braking current for the regen functionality. Finally, a digital oscilloscope is also connected to the two gate drives of the switching MOSFETs of one of the motor phases to allow for an analysis to be carried out of the switching behaviour of the VESC when operating in the regen mode. The built-up test setup in the lab is shown below in Figure 9.

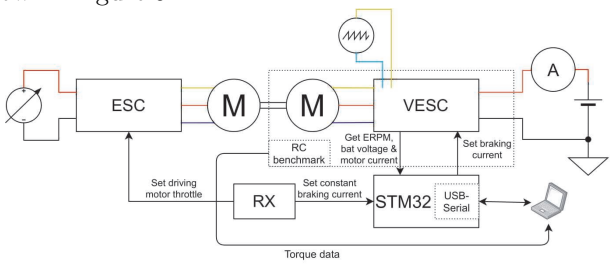

Fig. 8: Regenerative drivetrain test-setup diagram

The specifications of the used equipment can be found in Table 1.

5.4. *Expected results and outcome*

Various tests will be conducted where the regenerating brushless motor will be subjected to a range of RPMs, and requested regen current & power.

The following parameters will be logged:

- Braking current (I_{brake})
- Motor RPM (RPM)
- Battery regen current (I_{bat})
- Battery voltage (V_{bat})
- Motor torque (T)
- Driving motor/ESC voltage (V_{supply})
- Driving motor/ESC current (I_{supply})

With all of these parameters logged, it is possible to

Lab bench power supply	AFX-9660SB 0-30V 0-3A
Driving motor	Turnigy Aerodrive D2826/10 1400 KV
Driving ESC	YEP 40 A
Driven motor	EMAX GT2215/10 1100 KV
regen ESC	Maytech MTVESC50A VESC compatible
Torque measuring device	RC Benchmark Series 1580
LiPo battery	3D Robotics 3s 9C 5000 mAh

Table 1: Used equipment specifications

determine the approximate total drivetrain efficiency from the measurements to have a better estimate available of the practically achievable regen drivetrain efficiency, encompassing both the BLDC motor acting as a generator and the regen ESC. This can be done by comparing the mechanical power present at the coupled motor shaft to the electrical charging power of the battery. The mechanical and electrical power figures can easily be calculated from the measured parameters using the following formulae:

$$P_{mech} = T \cdot 2\pi \frac{RPM}{60} \tag{33}$$

$$P_{bat} = V_{bat} \cdot I_{bat} \tag{34}$$

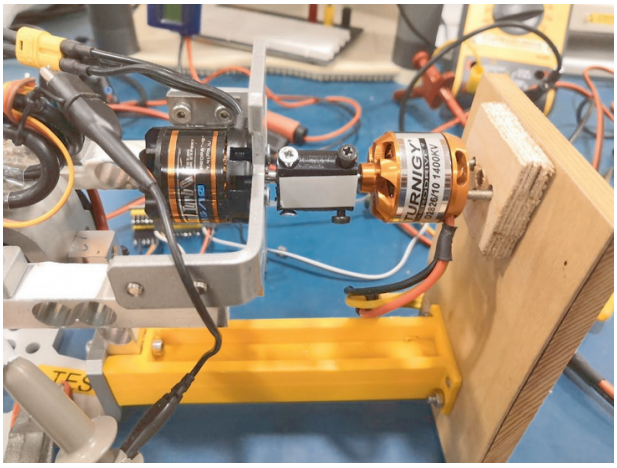

Fig. 9: regen drivetrain test-setup, with driving motor on the right and driven motor on the left, mounted on the RC Benchmark torque measuring device

5.5. *Observations during the test*

The main tests that were conducted involved determining the efficiency of the regen drivetrain for a range of RPMs and mechanical power. For each run, the driving motor ESC was set to keep the BLDC running at a constant RPM using the driving ESC's governer mode. For each constant RPM the requested braking current was gently increased, which lead to both the battery recharging power and the mechanical power on the motor shaft to increase. It was unfortunately not possible to choose constant measuring points for all RPMs with the same braking current or recharging power due to induced instabilities in the system probably caused by a conflict of the braking current control-loop of the VESC and the RPM governor of the driving ESC at certain operating conditions. Instead, it was opted to try to approach similar measuring points that resulted in stable readings to hopefully increase the accuracy of the measured data.

Another anomaly that was first observed was that the battery discharge current reported by the VESC didn't correspond with the external ammeter. After performing some additional measurements and checks it was found that the VESC had a near constant current reading error of around 0.25 A - 0.3 A when the brake current is set high enough to actually start the regen mode, which can be clearly seen in the graphed out measurements shown in Figure 10. The rest of the reported parameters logged by the VESC (motor RPM, battery voltage and motor current) were also able to be checked with a multimeter and did show good correspondence to the measured data.

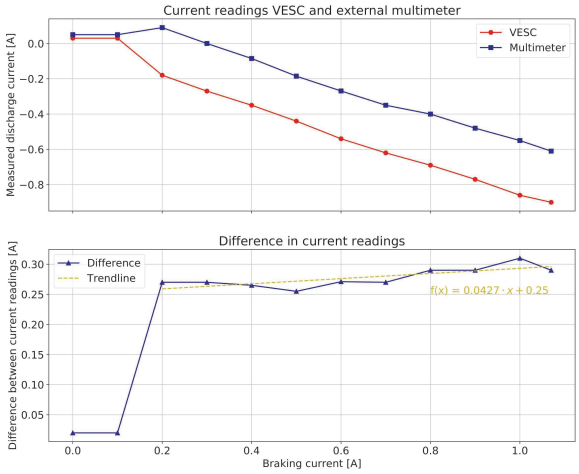

Fig. 10: VESC current measurement discrepancy

During the test the gate drive signals of the VESC of both the high- and low-side switching MOSFETs of one of the motor phases were probed to investigate the exact switching behaviour of the regen mode. Instead of using (body-)diodes to perform the diode functions, the VESC uses active rectification. This means it uses the MOSFETs

as semi-ideal diodes. This complicates the switching pattern and control logic, but can increase the overall efficiency by virtually eliminating the voltage drop due to the low on-resistance characteristics of power MOSFETs reducing the power dissipation significantly when compared to a regular diode.[12] An additional drawback of the active rectification approach is that a small amount of power is required every time the switching element has to change state, which at high frequencies and certain conditions may offset the power dissipation savings. The observed switching behaviour, together with the probing locations, is shown in Figure 11. Three distinct switching regimes can be observed in Figure 11b:

(1) Active rectification, allowing current flow to the battery when higher voltage is being generated by the inductors
(2) Switching element of boost converter
(3) Connecting phase to ground, making sure there is a complete current path

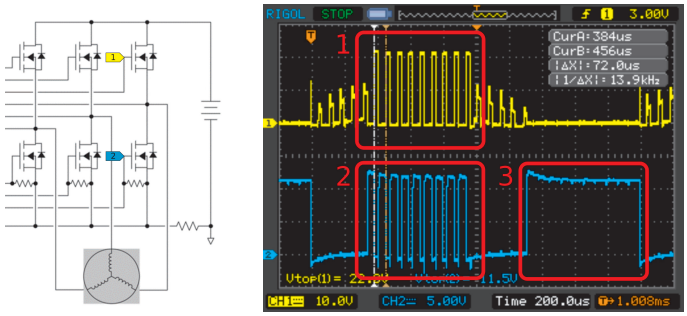

(a) Probing locations channel 1 & 2

(b) Oscilloscope screenshot of MOSFET gate switching pattern

Fig. 11: Switching behaviour of high- and low-level MOSFETs of motor phase during regen operation of VESC

5.6. *Results*

With all of the necessary data gathered and processed, the measurements at the different RPM ranges were grouped together and it's efficiency calculated using the formulae described in the test setup expected results and outcomes subsection (Subsection 5.4). The result of this for the first measurement series performed with a constant RPM of around 5000 is shown in Table 2.

The efficiency results of the drivetrain for the various RPM runs are plotted in Figure 12.

As was expected, the efficiency of the regen drivetrain varies considerably for different power levels & RPMs. This can be explained by the fact that the total efficiency figure is a combination of the efficiency of the BLDC motor to convert the mechanical shaft power to electrical power, and the electrical efficiency of the regen controller to convert the complex 3-phase lower AC-voltage to a higher DC-voltage suitable to safely charge the LiPo battery.

It can be clearly seen that the efficiency is very low at lower power levels. At very low power levels all of the regenerated power is used to supply the VESC itself, leaving little or no additional power for the battery to be recharged. This explains the zero efficiency number at low power values, since all of the recuperated energy is used to drive the regen controller itself, which in some cases is not even sufficient requiring still some power from the battery to drive the VESC.

The performance of the regen drivetrain generally increases with increasing mechanical input power levels. The very rapid increase in performance at the beginning of the curves can be partly explained by the phenomenon that was just described, but there are probably also other factors at play. At very low generator currents and power levels (BLDC) motors have a very low efficiency, which rapidly increases when the generator current only rises slightly.[13] The efficiency gains for higher input powers do taper off at a certain point. The optimum efficiency point will depend on both the characteristics of the BLDC motor being used as the generator, as well as the performance characteristics of the VESC switching hardware.

The final observation that can be made is that overall higher RPMs do seem to result in slightly higher efficiency figures. This can partly be explained by the fact that higher RPMs result in a higher input voltage to the VESC regen controller, which in turn has to boost the input voltage by a lower fraction to still achieve a high enough output voltage to charge the batteries. This means that for it to achieve the same charging power as with a lower RPM, less input current is required which leads to less heat losses due to resistance present in the windings, switching elements, etc.

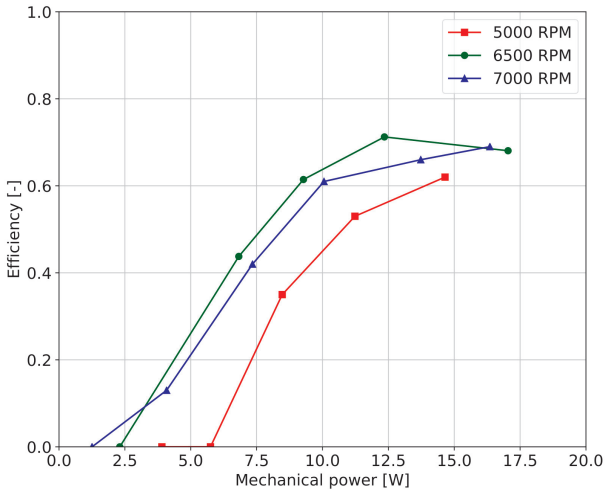

Fig. 12: Efficiency figures calculated from VESC test runs for different RPMs

6. Conclusion

A simplified wind-field model around obstacles such as circular and oval shaped hills was constructed based on potential flow theory. A model was developed to determine the

#	Time stamp	I_{supply}[A]	V_{supply} [V]	P_{supply} [W]	I_{bat} VESC [A]	$-I_{bat}$ (multi) [A]	Torque [N*m]
1	13/11/2020 17:23	0.72	8.9	5.7	0.01	−0.049	-0.0075
2	13/11/2020 17:24	0.99	9.0	8.9	−0.23	−0.007	-0.011
3	13/11/2020 17:25	1.38	8.9	13.6	−0.47	0.248	-0.0162
4	13/11/2020 17:26	1.82	8.9	18.4	−0.73	0.491	-0.0215
5	13/11/2020 17:27	2.30	8.9	24.5	−0.98	0.750	-0.028

#	ERPM	V_{bat} [V]	I_{brake} [A]	RPM	P_{mech} [W]	P_{bat} [W]	η
1	-34805	12.0	0.00	4972	3.905	−0.588	0%
2	-34935	12.0	0.60	4991	5.749	−0.084	0%
3	-34957	12.1	1.25	4994	8.472	3.001	35%
4	-34918	12.2	1.95	4988	11.23	5.990	53%
5	-34976	12.2	2.69	4997	14.65	9.150	62%

Table 2: Measured & calculated data for 5000 RPM run

maximum theoretical regeneration power if wind-hovering orographic soaring techniques are applied, given a certain wind-field and aerodynamic characteristics of the UAV. The resulting modular simulator program is able to determine the hovering locations and gives an estimate of the maximum achievable regeneration power. For the source wind-field, either the simplified potential-flow based model can be used, which needs very little computational power making it suitable to be even run on on-board processors of UAV's, or a wind-field generated by other more advanced software or even from a measurement field. The tool should allow anyone to easily get an estimate of the feasibility of the regenerative hovering soaring method in their particular application.

Furthermore, a working regenerative drivetrain test-setup that could be incorporated in a small electric UAV was tested and proved that with commercial source-able components a regenerative electric drivetrain can be constructed that has a mechanical input power to recharging power efficiency of up to 70 % at it's optimum operating conditions.

For future work, additional simulations could be carried out by simulating real-life conditions. The model can then be validated by performing a flight-test in these conditions with the devised regenerative drivetrain setup.

Acknowledgments

We would like to thank our colleagues from the Never-Landing Drone working group for their continued support, suggestions, ideas and feedback.

Appendix A UAV aerodynamic parameters used for simulation

S	1	m^2
C_{L_α}	5.7	rad^{-1}
α_{0L}	-4	°
A	6	-
e	0.8	-
C_{D_0}	0.05	-

Table A.1: UAV aerodynamic parameters for simulation

References

[1] N.R.J Lawrance and J.J. Acevedo and J.J Chung and J.L. Nguyen and D. Wilson and S. Sukkarieh, Long Endurance Autonomous Flight for Unmanned Aerial Vehicles, *AerospaceLab Journal.* **8** (2014).

[2] N.R.J Lawrance and S. Sukkarieh, Long Wind energy based path planning for a small gliding unmanned aerial vehicle, in *AIAA Guidance, Navigation, and Control Conference and Exhibit,* (Illinois, Chicago, 2009).

[3] R. Carvalho, Development of the regenerative soarer: Theoretical and Practical aspects, in *Congress of the International Council of the Aeronautical Sciences (ICAS),* (Minas Gerais, Belo Horizonte, 2018).

[4] P. MacCready, Regenerative battery-augmented soaring in *Self-Launching Sailplane Symposium,* (New-York, Elmira, 1998).

[5] A. Fisher and M. Marino and R. Clothier and S. Watkins and L. Peters and J.L. Palmer, Emulating avian orographic soaring with a small autonomous glider, *Bioinspiration and Biomimetics.* **11**(1) (2015).

[6] J.W. Langelaan, Long distance/duration trajectory optimization for small UAV's, in *AIAA Guidance, Navigation, and Control Conference,* (South Carolina, Hitlon Head, 2007).

[7] P.K. Kundu and I.M. Cohen, Chapter 6.4 in *Fluid Mechanics* (Academic Press, San Diego, California, 2002)

[8] S. Besio and A. Mazzino and C.F. Ratto, Long Endurance Autonomous Flight for Unmanned Aerial Vehicles, *Boundary-Layer Meteorology.* **107**(1) (2003).

[9] M. Ragheb and M. Adam, Wind Turbines Theory - The Betz Equation and Optimal Rotor Tip Speed Ratio in *Fundamental and Advanced Topics in Wind Power* (Intech, 2011), pp. 21.

[10] N. Gavrilovic and A. Mohamed and M. Marino and S. Watkins and J.M. Moschetta and E. Benard, Avian-inspired energy-harvesting from atmospheric phenom-

ena for small UAV's *Bioinspiration and Biomimetics.* **14**(1) (2019).

[11] G.J. May and A. Davidson and B. Monahov, Lead batteries for utility energy storage: A review, *Journal of Energy Storage* **15** (2018) pp. 145–157

[12] Texas Instruments, *Basics of Ideal Diodes* (TI, 2019), pp.1–22

[13] U. Kafader, *Maxon Motors as Generators* (Maxon group, 2020)